1-1-2017

Large-scale synthesis of ternary Sn5SbP3/C composite by ball milling for superior stable sodium-ion battery anode

Wenchao Zhang
University of Wollongong, wz990@uowmail.edu.au

Jianfeng Mao
Chinese Academy Of Sciences, jmao@uow.edu.au

Wei Kong Pang
University of Wollongong, wkpang@uow.edu.au

Zaiping Guo
University of Wollongong, zguo@uow.edu.au

Zhixin Chen
University of Wollongong, zchen@uow.edu.au

Large-scale synthesis of ternary Sn5SbP3/C composite by ball milling for superior stable sodium-ion battery anode

Abstract

Alloy-based materials (i.e. Sn, Sb, P) are promising candidates for sodium-ion battery (SIB) anodes, but they suffer from capacity decay during charge/discharge cycling due to the pulverization caused by their huge volume change. Nanostructures can slow down the capacity fade, but most of the synthesis methods of such nanostructured anodes are difficult to scale-up. Herein, a ternary Sn5SbP3/C composite was fabricated by a green, low cost, one-step and easily scalable ball-milling of elementary Sn, Sb, P, and C. The microstructure of the ball-milled powders consists of micrometric agglomerates of active nano Sn4P3 and SnSb and Sn particles. Carbon in the composite acts as a conducting matrix, and it does not only benefit to the ball milling efficiency, but also benefit to the cycle life of the electrode. Each of the active Sn4P3 and SnSb and Sn phases in the composite functions mutually as a buffer for the others. As a result, this ternary composite anode delivers a good capacity of 352 mA h g-1 at the current density of 2 A g-1, which is notably higher than that of the binary Sn4P3/C and SnSb/C composites produced under the same conditions.

Disciplines

Engineering | Physical Sciences and Mathematics

Publication Details

Zhang, W., Mao, J., Pang, W., Guo, Z. & Chen, Z. (2017). Large-scale synthesis of ternary Sn5SbP3/C composite by ball milling for superior stable sodium-ion battery anode. Electrochimica Acta, 235 107-113.

Large-scale synthesis of ternary Sn_5SbP_3/C composite by ball milling for superior stable sodium-ion battery anode

Wenchao Zhang,[a, b] Jianfeng Mao,[b,*] Wei Kong Pang,[b,c] Zaiping Guo[b], Zhixin Chen,[a,*]

[a] Engineering Materials Institute, School of Mechanical, Materials & Mechatronics Engineering, University of Wollongong, NSW 2500, Australia.

[b] Institute for Superconducting & Electronic Materials, University of Wollongong, Wollongong, NSW 2522, Australia.

[c] Australian Centre for Neutron Scattering, Australian Nuclear Science and Technology Organization, Locked Bag 2001, Kirrawee DC, NSW 2232, Australia.

* Corresponding authors

Jianfeng Mao: E-mail: jmao@uow.edu.au, T: +61 2 4221 5225, F: +61 2 4221 5630

Zhixin Chen: E-mail: zchen@uow.edu.au, T: +61 2 4221 4932, F: +61 2 4221 5474

Abstract

Alloy-based materials (i.e. Sn, Sb, P) are promising candidates for sodium-ion battery (SIB) anodes, but they suffer from capacity decay during charge/discharge cycling due to the pulverization caused by their huge volume change. Nanostructures can slow down the capacity fade, but most of the synthesis methods of such nanostructured anodes are difficult to scale-up. Herein, a ternary Sn_5SbP_3/C composite was fabricated by a green, low cost, one-step and easily scalable ball-milling of elementary Sn, Sb, P, and C. The microstructure of the ball-milled powders consists of micrometric agglomerates of active nano Sn_4P_3 and SnSb and Sn particles. Carbon in the composite acts as a conducting matrix, and it does not only benefit to the ball milling efficiency, but also benefit to the cycle life of the electrode. Each of the active Sn_4P_3 and SnSb and Sn phases in the composite functions mutually as a buffer for the others. As a result, this ternary composite anode delivers a good capacity of 352.2 mA h g^{-1} at the current density of 2 A g^{-1} , which is notably higher than that of the binary Sn_4P_3/C and SnSb/C composites produced under the same conditions.

Key words: Sodium-ion battery, alloy anode, low cost, large-scale

1. Introduction

Sodium-ion batteries (SIBs) have been attracting great interest recently due to the low cost and abundance of sodium resources, especially for applications in stationary energy storage.[1-16] The successful commercialization of SIBs does not only calls for the development of electrode materials with enhanced performance, but also scalable synthesis protocols.[17] Alloy-based materials are believed to be very promising candidates for SIB anodes due to their high gravimetric and volumetric capacities, and slightly higher thermodynamic potential. [1, 18, 19] For instance, group 14 (Sn, $Na_{15}Sn_4$, 847 mA h g^{-1}) and 15 elements (P, Na_3P, 2596 mA h g^{-1}; Sb, Na_3Sb, 660 mA h g^{-1}) based alloys[14, 20, 21] have been intensively studied recently and have showed promising properties. Nevertheless, large volume changes (> 200 %) are inevitable for these alloy anodes during sodiation/desodiation. The huge volume expansion will lead to continuous pulverization, particle cracking, and subsequent separation of the active materials from the current collector and result in fast capacity fade.[1, 2, 22]

Nanomaterials with designed and optimized structures can slow down the capacity fade. The use of these nanosized materials by industry in the near future is unlikely, however, because of their complicated synthesis procedures, very high synthesis costs, high surface reactivity, low tap density, and difficulties for large-scale synthesis. In contrast, ball milling is a simple, cheap, and easily scalable synthesis method, and hence, it has a potential for industrial-scale application. Binary composite systems such as Sn_4P_3 and SnSb formed via ball milling have been shown to have significantly better electrochemical performance over pristine Sn, Sb, or P.[20-3] The electrochemical performance of the ball milled binary Sn_4P_3 or SnSb is still far from adequate for practical applications, however, especially in terms of high rate

charging/discharging.[23-26]

Herein, we report a ternary Sn_5SbP_3/C composite synthesized via ball-milling, which contains Sn_4P_3, SnSb and Sn nanoparticles (NPs), which are in intimate contact with each other and form heterojunctions in a conductive carbon matrix. The ternary composite displays superior electrochemical performance to the binary Sn_4P_3/C or SnSb/C composite. It was found that the Sn and SnSb in the composite facilitate the electron transfer and Sn_4P_3 provides high sodium storage capacity. The SnSb phase also promotes a superior stable cycling performance by the formation of an intermediate amorphous phase Na_xSb.[23, 27-29] It seems that the superior electrochemical performance of the ternary Sn_5SbP_3/C composite is resulted from a synergetic effect of the multi phased nanostructure on a conductive network. Importantly ball milling is a scalable process and a large volume of composite architecture electrodes can be easily produced for practical applications.

2. Experimental Section

Preparation of Sn_5SbP_3/C ternary composite

Sn_5SbP_3/C powder was directly synthesized by ball milling the raw materials of Sn (Aldrich, ≥99.8%), Sb (Aldrich, ≥99.5%), red phosphorus (Aldrich, ≥99%) and carbon black. The weight ratio of Sn: Sb: P: C in the composite is 64.26:13.18:10.06:12.5. The ball milling was conducted in a planetary QM-1SP2 ball mill for 30 h at 500 rpm. A stainless steel jar and stainless steel balls of 10 mm in diameter are used. The powder-to-ball weight ratio was 1:30. For comparison, binary composites SnSb/C and Sn_4P_3/C were also synthesized under the same conditions. The weight ratios are Sn: Sb: C= 43.19: 44.31: 12.5 and Sn: P: C = 73.11: 14.39: 12.5 in the binary composites SnSb/C and Sn_4P_3/C respectively. The storage and handling of all the samples were performed in an Ar filled glovebox (MBraun Unilab).

Materials characterization

The phasic composition and information of the as-prepared powders were characterized by

powder X-ray diffraction (XRD) on a GBC MMA diffractometer with a Cu K_α radiation at a scanning rate of 1° min^{-1}. The particle morphology and size of the prepared powder materials were characterized on a JEOL JSM-7500FA field-emission scanning electron microscope (FESEM) and on a JEOL ARM-200F cold field emission and aberration-corrected transmission electron microscope (TEM).

Electrochemical measurements

Electrodes were fabricated using a slurry-coating method. The synthesized materials (Sn_5SbP_3/C, Sn_4P_3/C and SnSb/C) were mixed with Super P carbon black and carboxymethyl cellulose (CMC) in the weight ratio of 8:1:1 to form slurry with deionized (DI) water. Then, the slurry was coated on copper foil and dried in a vacuum oven at 80 ℃ for 12 h. Coin-type (CR2032) cells were assembled in an argon-filled glove box (H_2O < 0.1 ppm, O_2 <0.1 ppm), with 1 M $NaClO_4$ in a mixture of propylene carbonate (PC) with 5 wt. % fluoroethylene carbonate (FEC) as the electrolyte. Cyclic voltammetry (CV) tests were conducted on a Bio-logic VMP-3 electrochemical workstation at a scan rate of 0.05 mV s^{-1}. The cells were galvanostatically charged-discharged between 0.01 and 2.0 V versus Na/Na^+ at various current densities on a Land battery tester. The mass loading of active material (Sn_5SbP_3, Sn_4P_3 and SnSb) was over 0.78 mg cm^{-2}. The specific capacity was calculated based on the weight of pure Sn_5SbP_3, Sn_4P_3 and SnSb active materials.

3. Results and discussion

Fig. 1a presents the X-ray diffraction (XRD) patterns of the ternary Sn_5SbP_3/C and the binary Sn_4P_3/C and SnSb/C composites. The ternary Sn_5SbP_3/C composite contains three intermetallic and metallic phases: Sn_4P_3 (ICSD#15014), SnSb (ICSD#52303) and Sn (ICSD#40037). In contrast, only Sn_4P_3 or SnSb was observed in the binary composite Sn_4P_3/C or SnSb/C, respectively. The carbon black is not observed in the XRD patterns due to

its amorphous features, but it can be clearly identified by Raman analysis, as shown in Fig. S1 in the Supporting Information. Also, no bonds of C with Sn, Sb, and/or P are observed in X-ray photoelectron spectroscopy (XPS) analysis (Fig. S2). Fig. 1b presents the a Rietveld refinement profile for the Sn_5SbP_3/C composite, performed by using the GSAS-II software package.[30] All the peaks in the XRD pattern of the ternary Sn_5SbP_3/C can be indexed those of hexagonal Sn_4P_3 (R $\bar{3}$m), cubic SnSb (F m $\bar{3}$m), and tetragonal Sn ($I4_1/amd$). The lattice parameters obtained from the Rietveld refinement are a = 4.0283 Å, c = 35.6999 Å for the Sn_4P_3, a = 6.1278 Å for the SnSb and a = 5.8456 Å c = 3.1903 Å for the Sn respectively. The amount of each phase in the Sn_5SbP_3 was calculated as 65.75 ± 3.14 wt% Sn_4P_3, 18.54 ± 0.62 wt% SnSb, and 15.71 ± 0.67 wt% Sn.

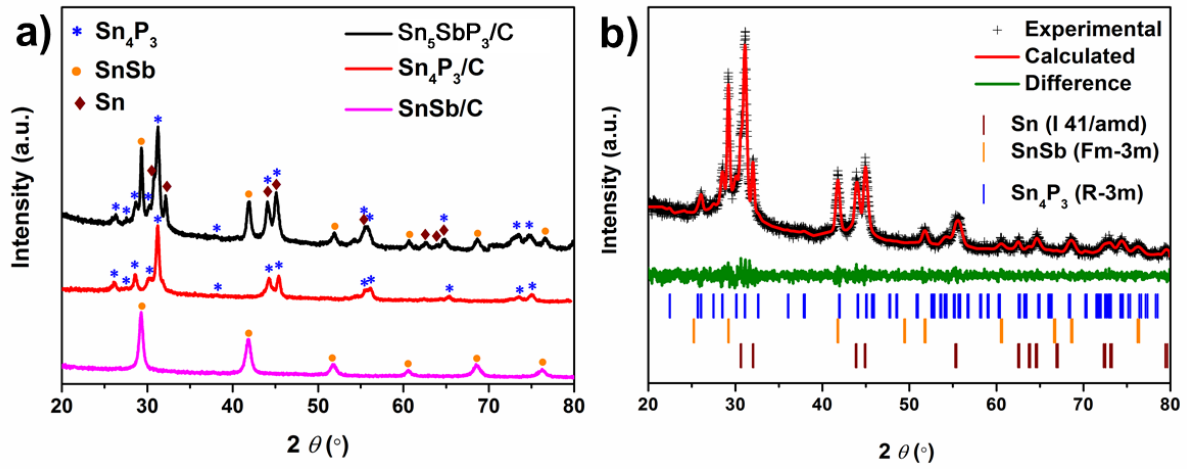

Fig.1. a) XRD patterns of Sn_5SbP_3/C composite, Sn_4P_3/C and SnSb/C; b) Rietveld refinement profile for the Sn_5SbP_3/C composite.

The as-milled Sn_5SbP_3/C, Sn_4P_3/C and SnSb/C powders were characterized by SEM and the results are shown in Fig 2. It can be seen that the powders in all three samples show irregular shapes in their morphology. The agglomerated and micro sized particles are the main constituent of the powders, and there are also numerous primary nanoparticles about 50 nm - 100 nm in size (Figs. 2a, b, c). The mixed structure of the micro- and nano- particles may allow full contact of the electrolyte with the active materials and hence facilitate an efficient

ion transportation.[31] It can also be seen that Sn, Sb, and P are distributed uniformly in the Sn_5SbP_3/C composite according to the energy dispersive X-ray spectroscopy (EDX) (Fig. 2d). EDX results for the Sn_4P_3/C and SnSb/C are shown in Fig. S3 and the compositions of the three different powders are listed in Table S1.

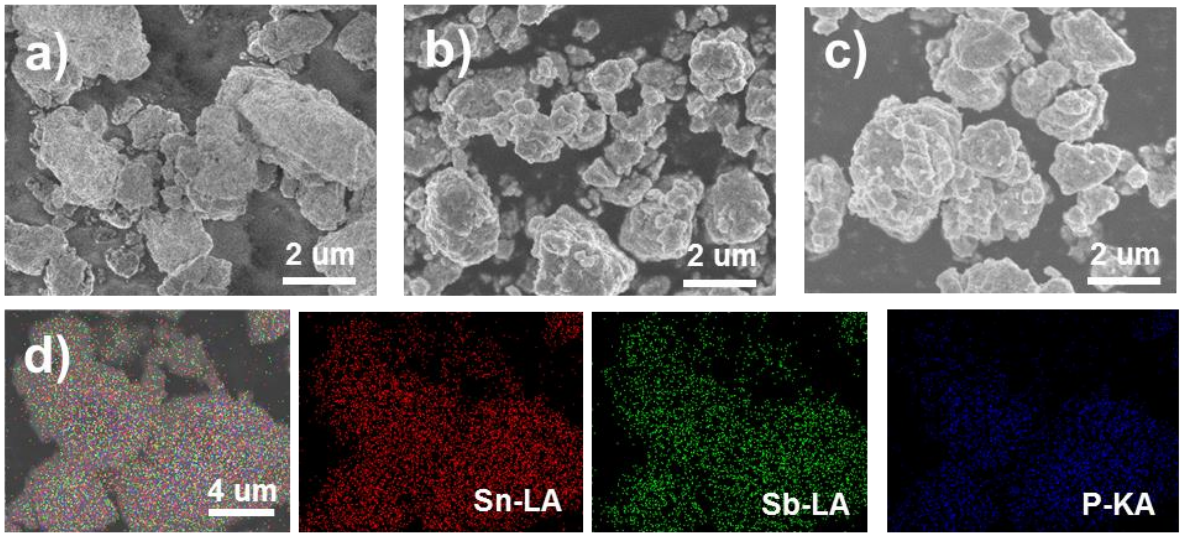

Fig.2. SEM images of a) Sn_5SbP_3/C composite, b) Sn_4P_3/C, c) SnSb/C powders; d) EDX mappings of Sn_5SbP_3/C composite.

Fig. 3 shows a TEM image, and a HRTEM image taken from a micron particle of the Sn_5SbP_3/C composite. The micron particle is composed of nanoparticles with the size ranging from 20 to 100 nm (Fig. 3a). These nanoparticles are composed of Sn_4P_3, SnSb and Sn and they are intimately mixed and uniformly distributed in the amorphous carbon matrix (Fig. 3b). The microscale particle size could make the power easy to handle and a higher tapped density, while the nanostructure provides short and fast ion diffusion path during sodiation and desodiation cycling. Figure 3b shows a HRTEM image of such a nanoparticle and the inset shows the indexed fast Fourier transform (FFT) pattern. From this pattern the lattice fringes were indexed and the spacings of the fringes were measured to be about 0.283 nm for the (107) planes and 0.309 nm for the (01 $\bar{5}$) planes. These values are in good agreement with the d_{107} and $d_{01\bar{5}}$ of Sn_4P_3. The Sn_4P_3 particle is about 20 nm in size and is also

surrounded by a few minor Sn and SnSb particles. The HRTEM observations are consistent with the XRD results and further confirm the coexistence of the three phases: Sn_4P_3, SnSb and Sn in the Sn_5SbP_3. It also should be noted that the phosphorus containing phase is sensitive to the electron beam and unstable at high voltages and at room temperature. Therefore, the lowest available voltage of 80 kV and a liquid nitrogen holder were used during the HRTEM measurements.

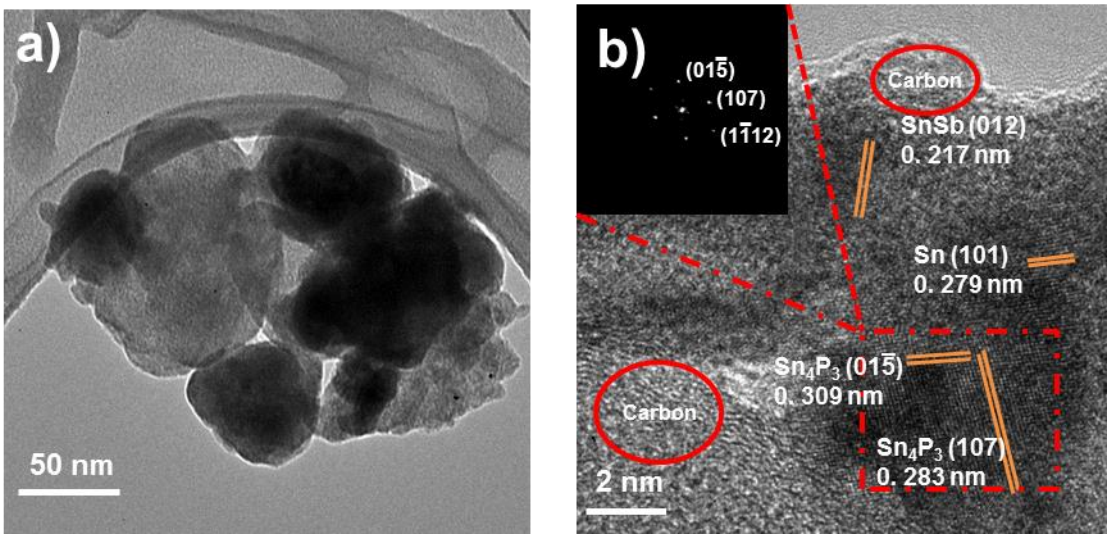

Fig. 3. a) TEM image of the Sn_5SbP_3/C composite, b) HRTEM image of the Sn_5SbP_3/C composite, with the inset showing the FFT pattern of the zone outlined in red.

The electrochemical performance in terms of sodium storage of the Sn_5SbP_3/C composite was systematically investigated. Fig. 4a displays cyclic voltammograms (CV) of the Sn_5SbP_3/C composite. During the first cathodic scan, a weak peak occurred at around 0.8 V, but it reduced slowly and disappeared in the following four cycles. This peak reduction may be attributed to the sodiation of amorphous phosphorus at the surface of the Sn_5SbP_3/C composite. The apparent reduction band at around 0.01-0.1 V may be attributed to the formation of $Na_{15}Sn_4$ and Na_3P, Na_3Sb (Eq. 1). In the second and subsequent cathodic scans, this large reduction band has obviously shrunken and another new reduction peak appeared at around 0.2-0.7 V. These two reduction bands at 0.18-0.69 V and 0.01-0.16 V can be attributed

to the Na-Sn, Na-Sb and Na-P alloying reactions (Eqs. 2, 3 and 4), according to the CV results for the Sn_4P_3/C and SnSb/C electrodes (Figs. S4a and b). During the anodic scans, the oxidation peaks at around 0.29 and 0.8 V are mainly attributed to the Na-Sn and Na-P de-alloying reactions (Eqs. 3 and 4), and the Na-Sn and Na-Sb de-alloying reactions (Eqs. 2 and 4), respectively. The main peak at around 0.6 V is due to the desodiation of Na_3P, although some overlap of the Na-Sn and Na-Sb de-alloying reactions may also be present. Therefore, it is likely that the sodiation and desodiation mechanism may proceed as follows:

During the initial charging (Na insertion) process

$$Sn_4P_3 + SnSb + Sn + 34.5Na^+ + 34.5e^- \rightarrow 1.5Na_{15}Sn_4 + 3Na_3P + Na_3Sb \quad (1)$$

In the subsequent discharging (sodiation) and charging (desodiation) processes

$$Sb + 3Na^+ + 3e^- \leftrightarrow Na_3Sb \quad (2)$$

$$P + 3Na^+ + 3e^- \leftrightarrow Na_3P \quad (3)$$

$$Sn + 3.75Na^+ + 3.75e^- \leftrightarrow Na_{3.75}Sn \quad (4)$$

The theoretical capacity of Sn_5SbP_3, Sn_4P_3 and SnSb could be calculated as 996.3, 1130.5 and 753.8 mA h g^{-1}, respectively. Fig. 4b shows the rate performance of the three electrodes (Sn_5SbP_3/C, Sn_4P_3/C and SnSb/C) at current densities of 100, 250, 500, 1000 and 2000 mA g^{-1}. Clearly, the rate performance of the Sn_5SbP_3/C is better than that of those Sn_4P_3/C or SnSb/C. Moreover, it seems that the superior sodium storage performance of the ternary composite to the binary composites becomes even more outstanding at the higher current densities. For example, a capacity of 352.2 mA h g^{-1} is obtained for the Sn_5SbP_3/C at the current density of 2 A g^{-1}, which is much larger than those of the two binary composite at the same current density. The capacity retention ratio of the Sn_5SbP_3/C composite electrode is 57.9 % which is also higher than 42.02% of the Sn_4P_3/C and 48.96% of the SnSb/C at the same current density of 2 A g^{-1}, as shown in Fig. 4c.

To better understand the reasons for the superior performance of the Sn_5SbP_3/C electrode, electrochemical impedance spectroscopy (EIS) was also conducted on the three electrodes

and compared, as shown in Fig. 4d. The EIS curves contain a depressed semicircle in the high frequency region, and a straight sloping line in the low frequency region. The resistor R_{ct} in parallel with the constant phase element (CPE) in the equivalent circuit is the charge-transfer resistance at the electrode/electrolyte interface, which is calculated from the depressed semicircle. Clearly, the R_{ct} of the Sn_5SbP_3/C electrode (110 Ω) is much lower than those of the binary electrodes (468 Ω for Sn_4P_3/C and 1439 Ω for SnSb/C). The lower the R_{ct} value is, the faster the ion transportation. Thus, the Sn_5SbP_3/C electrode has the fastest reaction kinetics among the three electrodes.

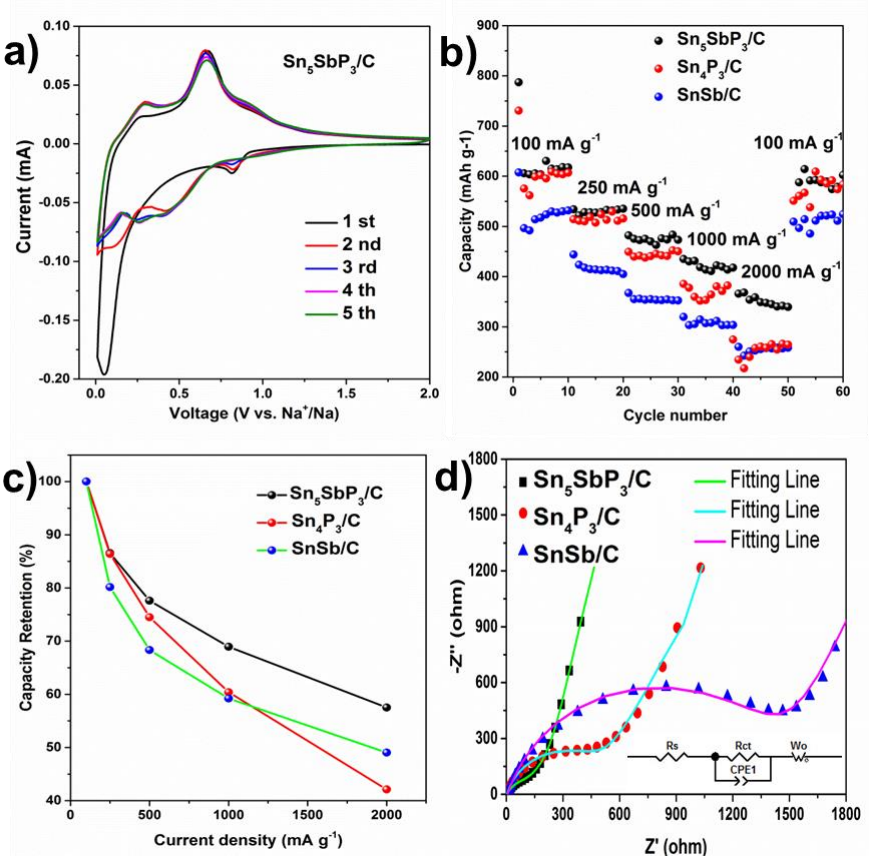

Fig. 4. (a) Cyclic voltammograms (CVs) of Sn_5SbP_3/C composite for the first 5 cycles, tested at a scanning rate of 0.05 mV s^{-1}, b) rate performance of the three electrodes at current densities from 100 mA g^{-1} to 2000 mA g^{-1}, c) average discharge capacity retention for the 3 electrodes at current densities from 100 mA g^{-1} to 2000 mA g^{-1}, and d) EIS spectra of the three electrodes.

To further explore the superior electrochemical performance of the Sn_5SbP_3/C composite, the long-term cycling stability of the three samples was investigated and compared, as shown in Fig. 5. The Sn_5SbP_3/C electrode exhibits a relatively more stable cycling performance at 500 mA g^{-1} (Fig 5a). A capacity of 431.6 mA h g^{-1} is delivered by the Sn_5SbP_3/C after the 200 cycles, which is higher than 346.4 mA h $g^{-1}$of the Sn_4P_3/C and 269.5 mA h g^{-1} of the SnSb/C after the same number of cycles. Meanwhile, the retention rates with respect to their second cycle capacities are 77.65% and 69.74%, for the Sn_4P_3/C and SnSb/C respectively and they are much lower than that of Sn_5SbP_3/C electrode (95.2% of the second cycle capacity). Accordingly, the discharge-charge profiles of the three electrodes at the current density of 500 mA g^{-1} at the 1^{st}, 2^{nd}, 50^{th}, 100^{th} and 200^{th} cycles are presented in Figs. 5b-d, respectively. The profiles display a long plateau at around 0.01-0.3 V (Sn_5SbP_3/C), 0.01-0.5 V (Sn_4P_3/C) and 0.2-0.3 V (SnSb/C), respectively, in their first discharge process. The plateaus are mainly due to the formation of the SEI layer. Several discharge and charge plateaus are observed after cycling, however. These results are in agreement with the CV results (Fig. 4a, Fig. S4a, b), and reflect the stepwise alloy phase transition reactions (Eqs. 2-4). The Sn_5SbP_3/C composite electrode also exhibits higher and more stable capacities than the binary composite electrodes at the higher current density (1 A g^{-1}), as shown in Fig. 5e. A capacity of 370.5 mA h g^{-1} is delivered by the Sn_5SbP_3/C composite in the 200^{th} cycle, which is higher than 251.5 mA h g^{-1} of the Sn_4P_3/C and 106 mA h g^{-1} of the SnSb/C in the same number of cycles.

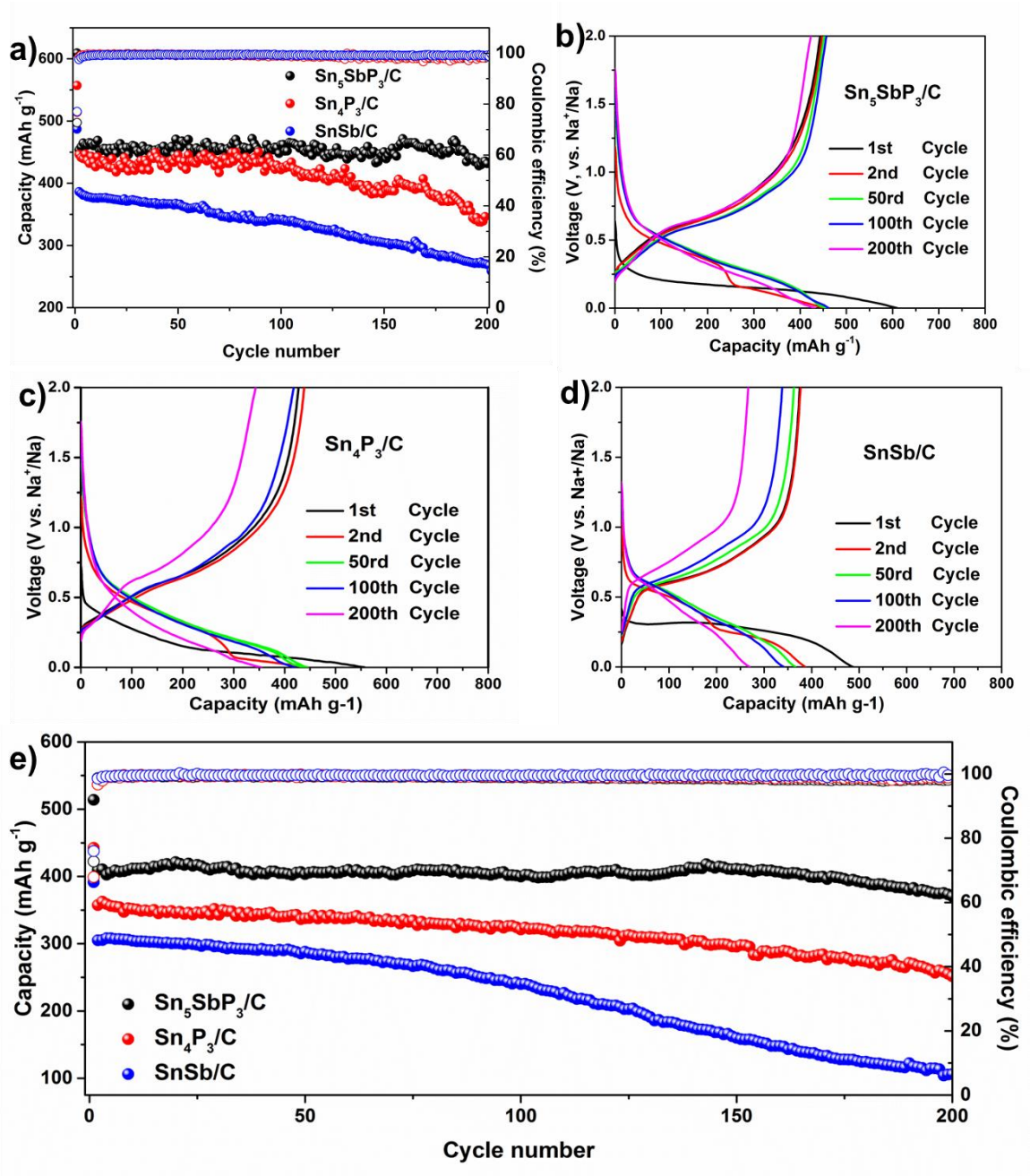

Fig. 5. (a) Cycling performance and Coulombic efficiency of three different materials tested at a current density of 500 mA g^{-1} in the range of 0.01-2V (vs. Na^+/Na). Galvanostatic charge-discharge curves of (b) Sn_5SbP_3/C composite, (c) Sn_4P_3/C and (d) SnSb/C for the 1st, 2nd, 50th, 100th and 200th cycles tested at current density of 500 mA g^{-1} in the range of 0.01-2V (vs. Na^+/Na) (e) Cycling performance and Coulombic efficiency of Sn_5SbP_3/C, Sn_4P_3/C and SnSb/C tested at a current density of 1000mA g^{-1} in the range of 0.01-2V (vs. Na^+/Na).

It is well known that one of the deadly problems for alloy-based anodes in SIBs is the huge

volume expansion during charging/discharging , which leads to continuous pulverization upon cycling[32, 33] Therefore, the morphology changes before and after 100 cycles were examined by SEM, as shown in Figs. 6 a - f. The Sn_5SbP_3/C composite electrode shows no obvious morphological change and only a few micro cracks were observed after 100 cycles. The Sn_4P_3/C and SnSb/C electrodes, however, show not only more cracks, but these cracks are also much coarser. Some of the cracks can be as wide as 5 μm and hundreds of micrometers long after 100 cycles. The results indicate that the volume changes are alleviated effectively in the ternary composite, and hence, it has the superior electrochemical performance.

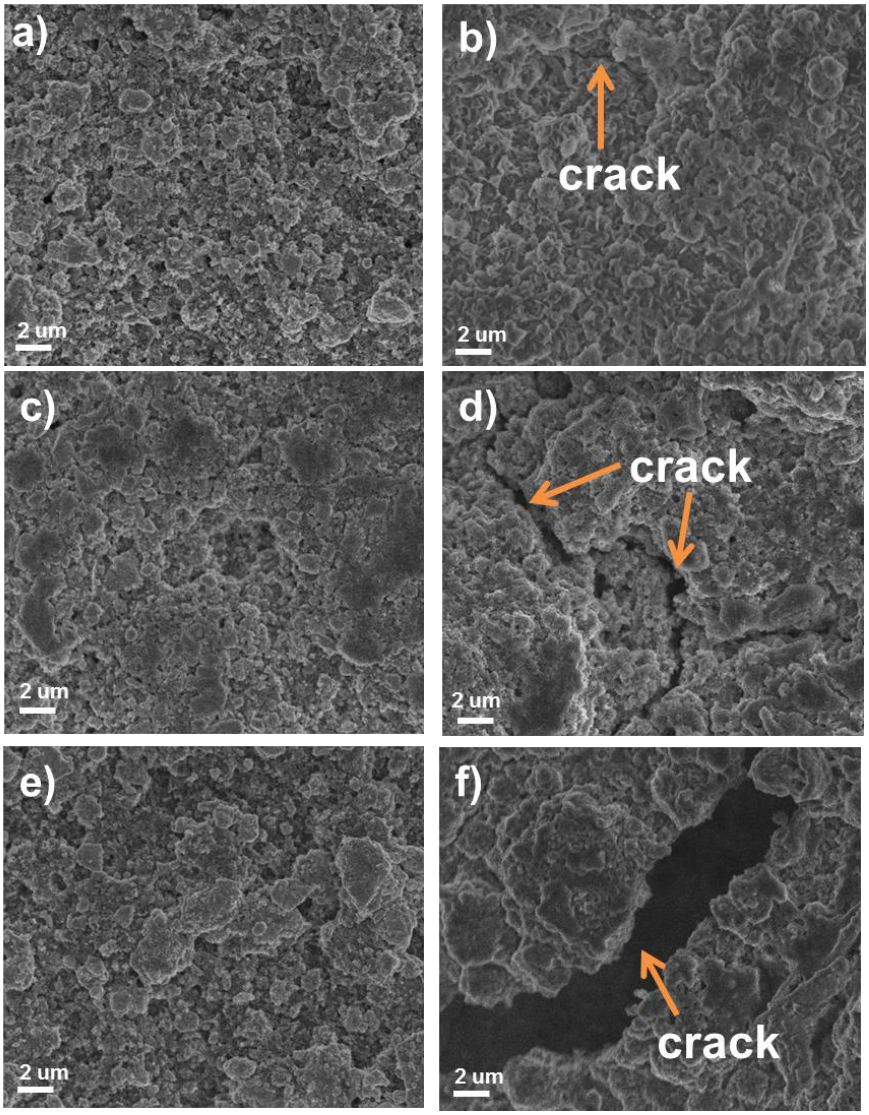

Fig. 6. FESEM image of a) fresh Sn_5SbP_3/C electrode, b) Sn_5SbP_3/C composite after 100

cycles at 1000 mA g^{-1}, c) fresh Sn_4P_3/C electrode, d) Sn_4P_3/C composite after 100 cycles at 1000 mA g^{-1}, e) fresh SnSb/C electrode, and f) SnSb/C composite after 100 cycles at 1000 mA g^{-1}

The superior electrochemical performance of the ternary Sn_5SbP_3/C composite can be attributed to its unique structure, where the Sn_4P_3, SnSb and Sn nanoparticles (NPs) are in intimate contact with each other and form heterojunctions in the conductive carbon matrix. The three phases may play different and complemental roles in the ternary Sn_5SbP_3/C composite electrode because that the Sn_4P_3 phase has a high capacity but a very low electrical conductivity, the Sn and SnSb should have good electric conductivity. (Table S2). Therefore the Sn and SnSb phases together with the conductive carbon matrix could form continuous conductive networks for faster diffusion of electrons[23] which in turn improves the electrochemical performance of the Sn_4P_3. The Sn_4P_3 and SnSb have different reaction potentials according to the CV results (Fig. 4a and S4). Therefore it is expected that the reaction products of Na_xSn, Na_ySb and Na_zP in the ternary composite electrode would act as buffers to support each other and moderate the volume expansion during cycling.[23, 25, 34] Furthermore, the three phases can form heterojunctions in the interfacial areas (Fig. 3), which will induce an electric field within the nanocrystals, and hence encourage a rapid interfacial ion/electron transfer.[17] In addition to the three active phases, the carbon in the composite can play an important role as well. The effect of the carbon content in the ternary Sn_5SbP_3/C composite on the Sn_5SbP_3/C composite was also investigated and the results are shown in Fig. S5. It seems that that the optimum carbon addition in the ternary Sn_5SbP_3/C composite is 12.5 wt. %. Considering that the carbon black only delivers a capacity of around 100 mA h g^{-1} (Fig. S6), the capacity in the Sn_5SbP_3/C composite is largely attributed from the three active phases. Nevertheless, the addition of carbon can benefit the cycle life due to its good electric conductivity and buffer effect (Fig. S5). The last, but still important, benefit brought by the

nano sized multiphase structure of the Sn_5SbP_3/C electrode is efficient Na ion transportation, which in turn enhances the performance of the electrode. All these factors synergistically contribute to better capacity and cycling performance and high rate capability by offering high electrical conductivity, fast ion transportation and high structure strength.

4. Conclusions

In summary, Sn_5SbP_3/C composite was successfully synthesized by a facile ball-milling technique. When tested as anode in sodium-ion batteries, the Sn_5SbP_3/C shows a superior electrochemical performance to the binary Sn_4P_3/C or SnSb/C electrode, especially at higher current densities (500 mA g^{-1} and 1000 mA g^{-1}). The excellent electrochemical performance of the Sn_5SbP_3/C electrode arises from a synergetic effect, which is due to the mutual buffering effect of the multiple phases, the fine grain size of the active phases, the conductive carbon matrix which enhances the integrity and the good electrical conductivity of the electrode. Our results encourage the exploration of superior cycle stable alloy based anode materials through the low-cost, eco-friendly, and scalable ball milling method for rechargeable batteries.

Acknowledgements

Authors would like to thank Dr. Tania Silver for the reading and editing of the manuscript, and also acknowledge the use of the ARC facilities purchased through FT150100109 and the ARC facilities in the Electron Microscopy Centre of the University of Wollongong (UOW), especially thanks Dr. Gilberto Casillas-Garcia for low temperature HRTEM. The author, Wenchao Zhang, would like to thank the UOW and Engineering Materials Institute of UOW for financial support.

References

[1] M.D. Slater, D. Kim, E. Lee, C.S. Johnson, Advanced Functional Materials, 23 (2013) 947-958.

[2] C. Bommier, X. Ji, Israel Journal of Chemistry, 55 (2015) 486-507.
[3] N. Yabuuchi, K. Kubota, M. Dahbi, S. Komaba, Chemical reviews, 114 (2014) 11636-11682.
[4] V. Palomares, M. Casas-Cabanas, E. Castillo-Martínez, M.H. Han, T. Rojo, Energy & Environmental Science, 6 (2013) 2312-2337.
[5] Y. Wen, K. He, Y. Zhu, F. Han, Y. Xu, I. Matsuda, Y. Ishii, J. Cumings, C. Wang, Nature communications, 5 (2014).
[6] S.Y. Hong, Y. Kim, Y. Park, A. Choi, N.-S. Choi, K.T. Lee, Energy & Environmental Science, 6 (2013) 2067-2081.
[7] H. Pan, Y.-S. Hu, L. Chen, Energy & Environmental Science, 6 (2013) 2338-2360.
[8] W. Zuo, W. Zhu, D. Zhao, Y. Sun, Y. Li, J. Liu, X.W.D. Lou, Energy & Environmental Science, 9 (2016) 2881-2891.
[9] L.P. Wang, L. Yu, X. Wang, M. Srinivasan, Z.J. Xu, Journal of Materials Chemistry A, 3 (2015) 9353-9378.
[10] Y. Xiao, H. Jang-Yeon, Y.-K. Sun, Journal of Materials Chemistry A, (2016).
[11] J. Chen, G. Zou, H. Hou, Y. Zhang, Z. Huang, X. Ji, Journal of Materials Chemistry A, 4 (2016) 12591-12601.
[12] X. Xu, D. Yu, H. Zhou, L. Zhang, C. Xiao, C. Guo, S. Guo, S. Ding, Journal of Materials Chemistry A, 4 (2016) 4375-4379.
[13] H. Hou, C.E. Banks, M. Jing, Y. Zhang, X. Ji, Advanced Materials, 27 (2015) 7861-7866.
[14] M.K. Datta, R. Epur, P. Saha, K. Kadakia, S.K. Park, P.N. Kumta, Journal of Power Sources, 225 (2013) 316-322.
[15] D.-H. Nam, K.-S. Hong, S.-J. Lim, H.-S. Kwon, Journal of Power Sources, 247 (2014) 423-427.
[16] D. Yan, X. Xu, T. Lu, B. Hu, D.H. Chua, L. Pan, Journal of Power Sources, 316 (2016) 132-138.
[17] Y. Zheng, T. Zhou, C. Zhang, J. Mao, H. Liu, Z. Guo, Angewandte Chemie International Edition, 55 (2016) 3408-3413.
[18] D. Kundu, E. Talaie, V. Duffort, L.F. Nazar, Angewandte Chemie International Edition, 54 (2015) 3431-3448.
[19] E.M. Lotfabad, J. Ding, K. Cui, A. Kohandehghan, W.P. Kalisvaart, M. Hazelton, D. Mitlin, Acs Nano, 8 (2014) 7115-7129.
[20] J. Qian, X. Wu, Y. Cao, X. Ai, H. Yang, Angewandte Chemie, 125 (2013) 4731-4734.
[21] A. Darwiche, C. Marino, M.T. Sougrati, B. Fraisse, L. Stievano, L. Monconduit, Journal of the American Chemical Society, 134 (2012) 20805-20811.
[22] J. Liu, P. Kopold, C. Wu, P.A. van Aken, J. Maier, Y. Yu, Energy & Environmental Science, 8 (2015) 3531-3538.
[23] I.T. Kim, S.-O. Kim, A. Manthiram, Journal of Power Sources, 269 (2014) 848-854.
[24] J. Mao, X. Fan, C. Luo, C. Wang, ACS applied materials & interfaces, 8 (2016) 7147-7155.
[25] J. Qian, Y. Xiong, Y. Cao, X. Ai, H. Yang, Nano letters, 14 (2014) 1865-1869.
[26] L. Ji, W. Zhou, V. Chabot, A. Yu, X. Xiao, ACS applied materials & interfaces, 7 (2015) 24895-24901.
[27] L. Baggetto, H.-Y. Hah, J.-C. Jumas, C.E. Johnson, J.A. Johnson, J.K. Keum, C.A. Bridges, G.M. Veith, Journal of Power Sources, 267 (2014) 329-336.
[28] Y. Kim, Y. Park, A. Choi, N.S. Choi, J. Kim, J. Lee, J.H. Ryu, S.M. Oh, K.T. Lee, Advanced materials, 25 (2013) 3045-3049.
[29] Q. Li, Z. Li, Z. Zhang, C. Li, J. Ma, C. Wang, X. Ge, S. Dong, L. Yin, Advanced Energy Materials, 6 (2016).
[30] B.H. Toby, R.B. Von Dreele, Journal of Applied Crystallography, 46 (2013) 544-549.
[31] W. Li, S.L. Chou, J.Z. Wang, J.H. Kim, H.K. Liu, S.X. Dou, Advanced Materials, 26 (2014) 4037-4042.
[32] H. Kang, Y. Liu, K. Cao, Y. Zhao, L. Jiao, Y. Wang, H. Yuan, Journal of Materials Chemistry A, 3 (2015) 17899-17913.
[33] P.R. Abel, M.G. Fields, A. Heller, C.B. Mullins, ACS applied materials & interfaces, 6 (2014) 15860-15867.
[34] L. Xiao, Y. Cao, J. Xiao, W. Wang, L. Kovarik, Z. Nie, J. Liu, Chemical Communications, 48 (2012) 3321-3323.

Large-scale synthesis of Sn_5SbP_3/C composite by ball milling for superior stable sodium-ion battery anode

Wenchao Zhang,[a, b] Jianfeng Mao,[b,*] Wei Kong Pang,[b,c] Zaiping Guo[b], Zhixin Chen,[a,*]

[a] Engineering Materials Institute, School of Mechanical, Materials & Mechatronics Engineering, University of Wollongong, NSW 2500, Australia.

[b] Institute for Superconducting & Electronic Materials, University of Wollongong, Wollongong, NSW 2522, Australia.

[c] Australian Centre for Neutron Scattering, Australian Nuclear Science and Technology Organization, Locked Bag 2001, Kirrawee DC, NSW 2232, Australia.

* Corresponding authors

Jianfeng Mao: E-mail: jmao@uow.edu.au, T: +61 2 4221 5225, F: +61 2 4221 5630

Zhixin Chen: E-mail: zchen@uow.edu.au, T: +61 2 4221 4932, F: +61 2 4221 5474

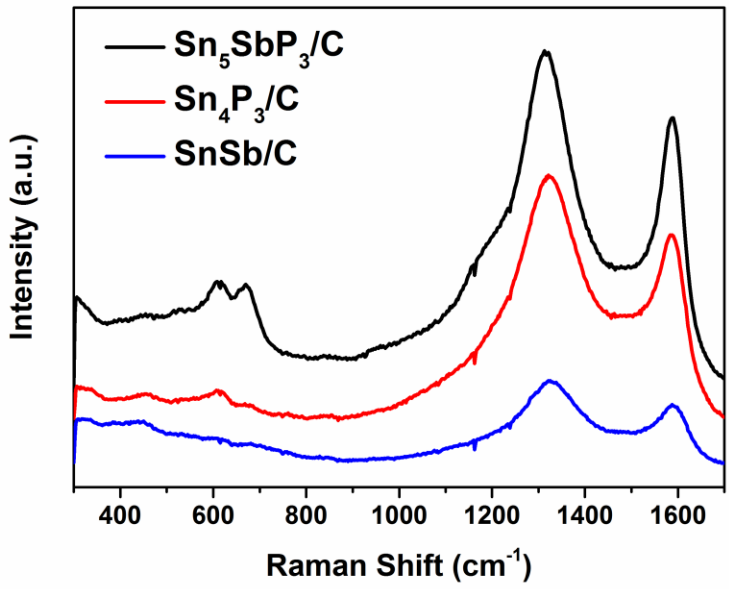

Fig.S1 Raman spectra of Sn_5SbP_3/C, Sn_4P_3/C and SnSb/C powder

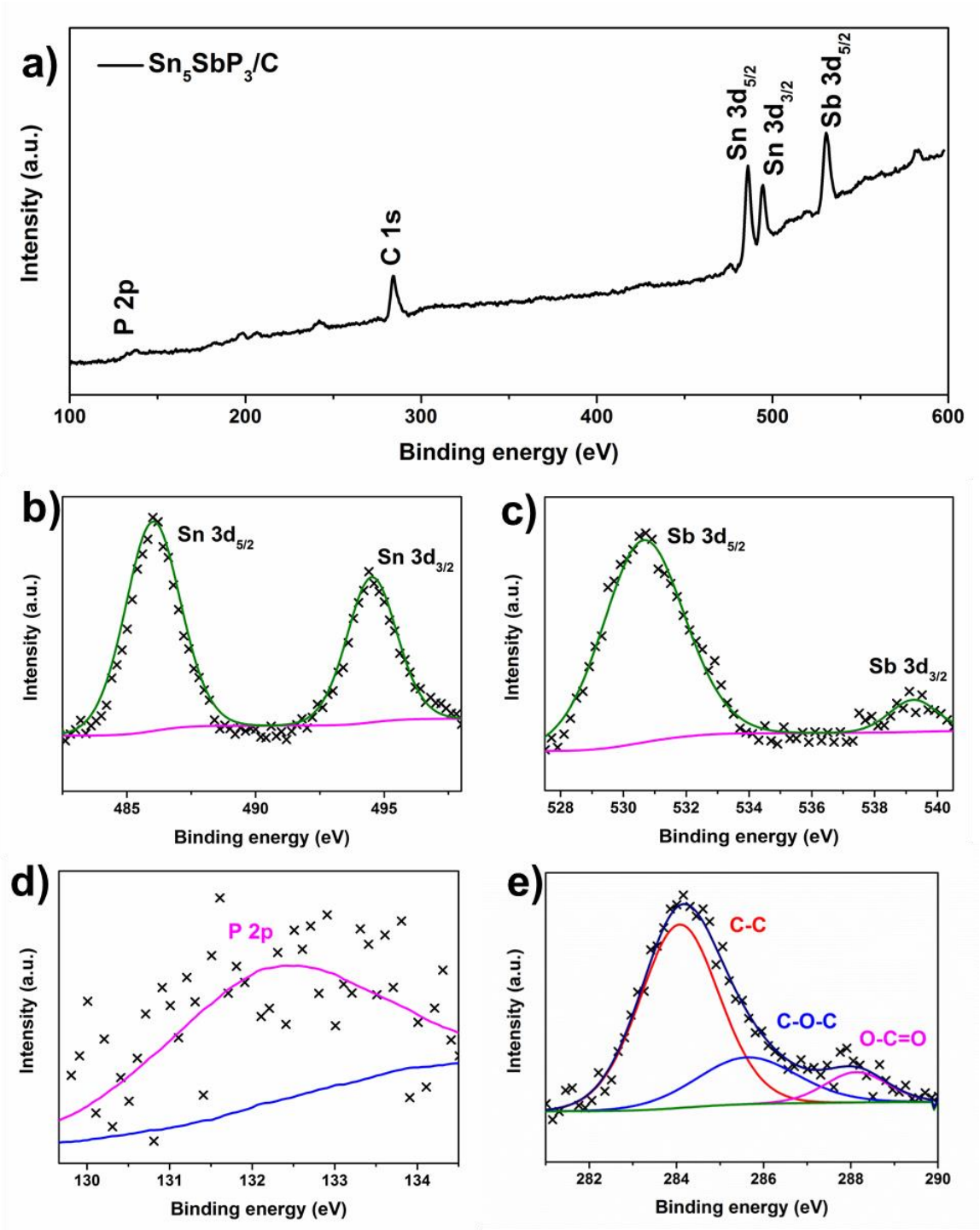

Fig. S2 a) Typical XPS survey spectra of the Sn_5SbP_3/C and the corresponding b) Sn 3d c) Sb 3d d) P 2p and e) C 1s XPS spectra

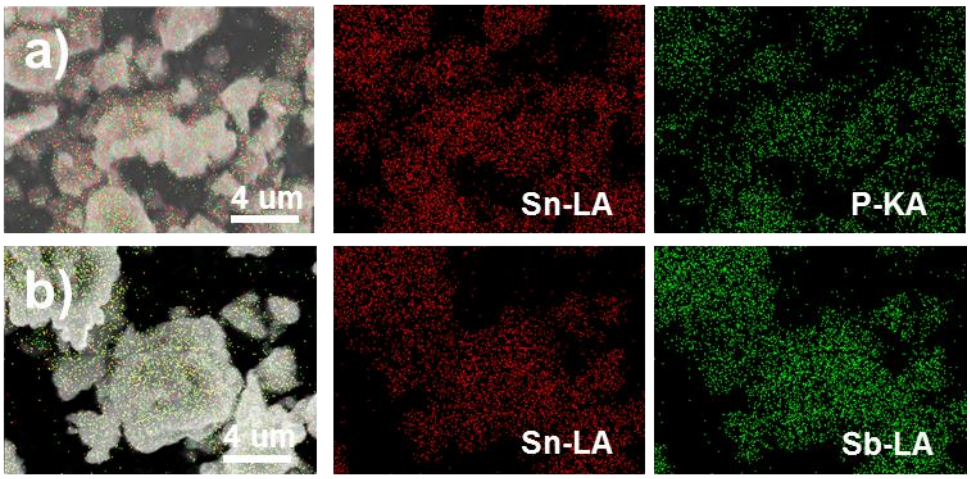

Fig. S3 EDS mapping of a) Sn_4P_3/C, b) SnSb/C powders

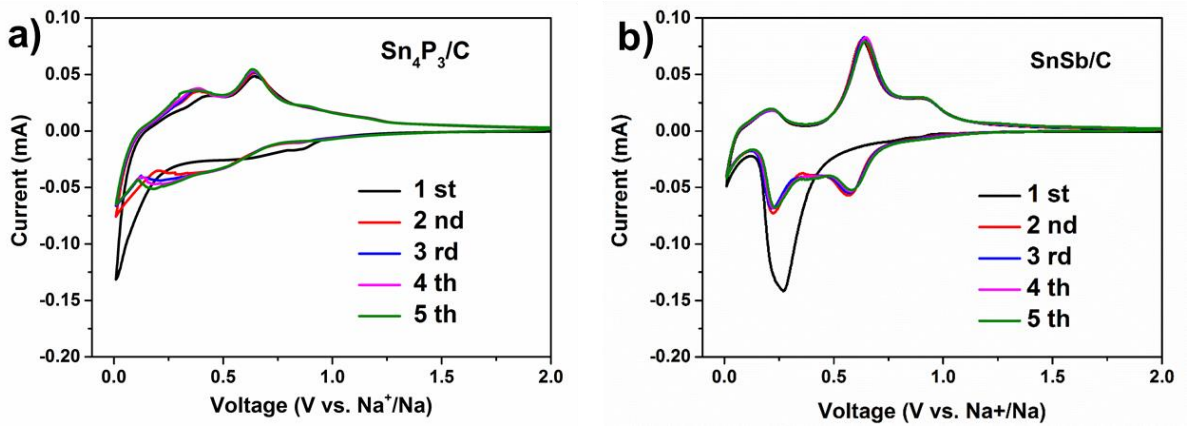

Fig. S4 Cyclic voltammograms of a) Sn_4P_3/C, b) SnSb/C electrodes tested at a scanning rate of 0.05 mV/s

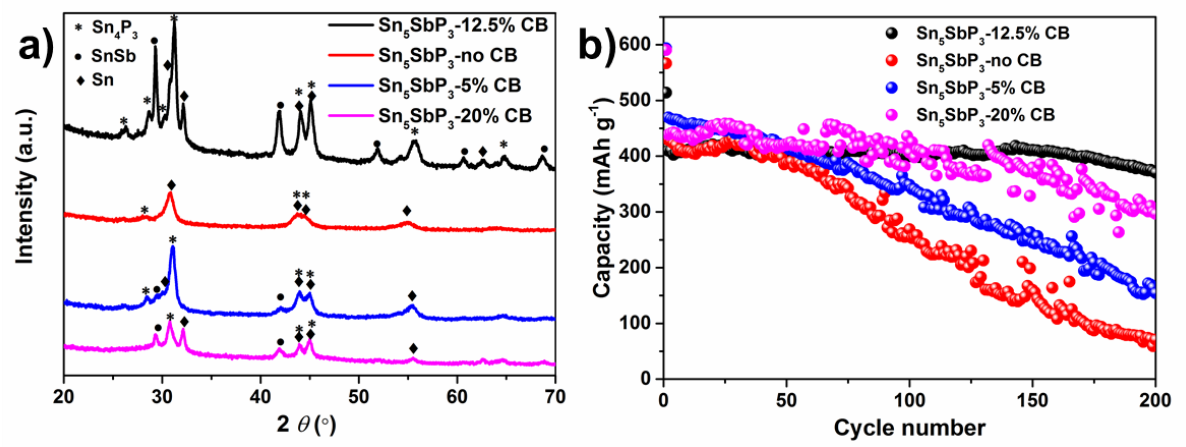

Fig. S5 a) X-ray diffraction (XRD) patterns and b) Cycling performance at the current density of 1A g^{-1} of Sn_5SbP_3-12.5% carbon black (CB), Sn_5SbP_3-no carbon, Sn_5SbP_3-5% carbon and Sn_5SbP_3-20% carbon

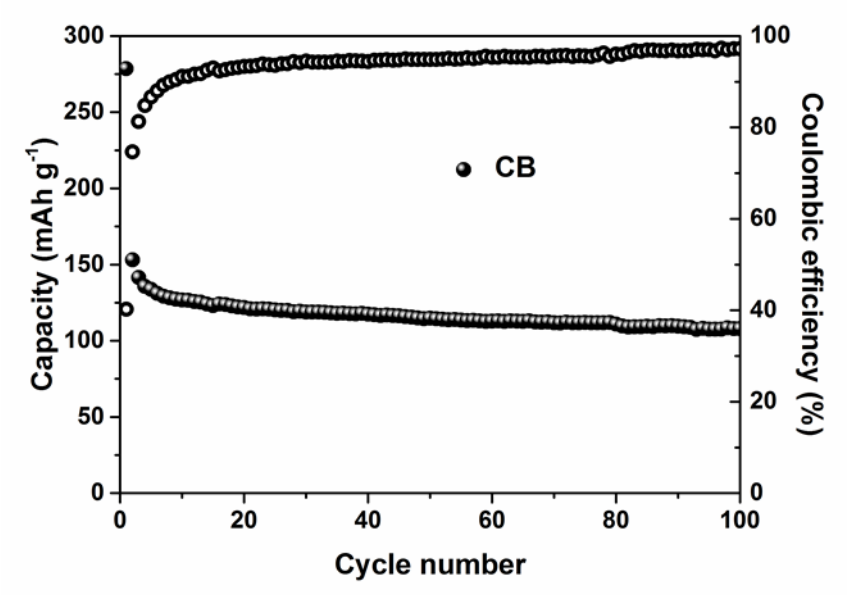

Fig. S6 Cycling performance of carbon black (CB) at the current density of 100 mA g^{-1}

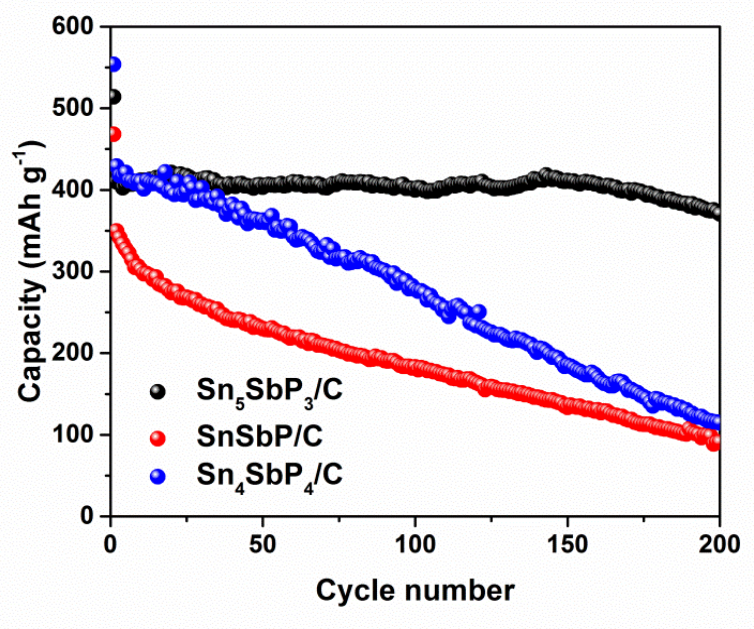

Fig. S7 Cycling performance at the current density of 1A g^{-1} of Sn_5SbP_3/C, SnSbP/C and Sn_4SbP_4/C

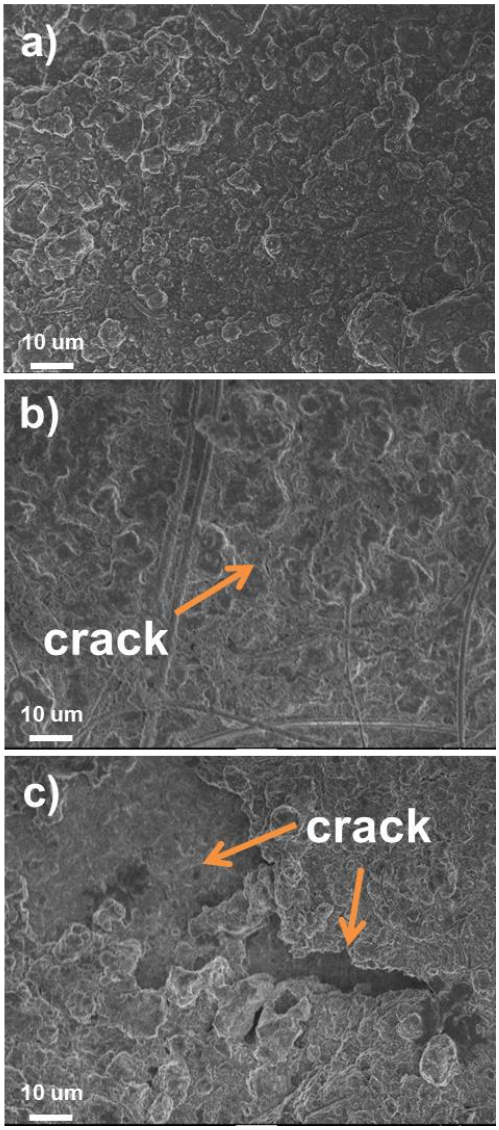

Fig. S8 FESEM images (1000X) of a) Sn_5SbP_3/C, b) Sn_4P_3/C, c) SnSb/C after 100 cycles at 1000 mA g^{-1}

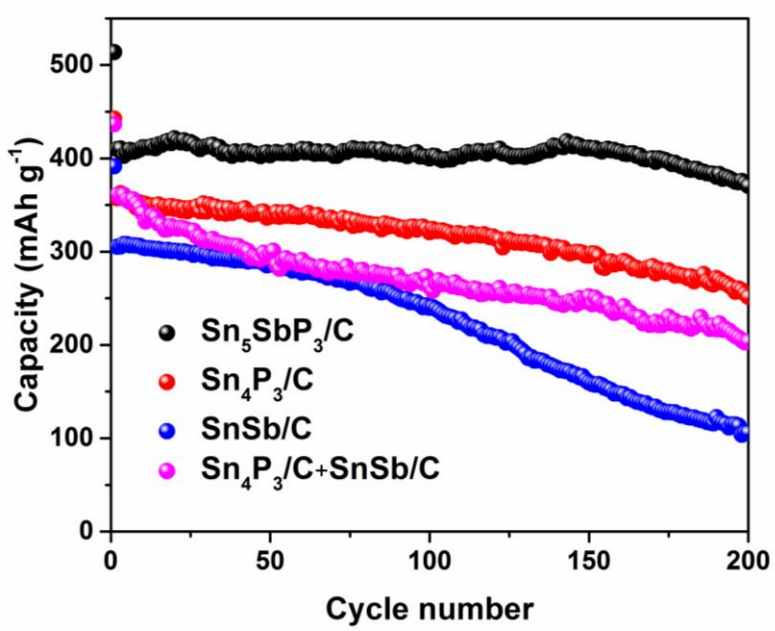

Fig. S9 Cycling performance at the current density of 1 A g^{-1} of Sn_5SbP_3/C, Sn_4P_3/C, SnSb/C and Sn_4P_3/C+SnSb/C

Table S1 EDS mapping composition of three different powders in wt.%

	Sn-LA	Sb-LA	P-KA
Sn_5SbP_3/C	73.55	16.31	10.13
Sn_4P_3/C	86.24		13.76
SnSb/C	48.82	51.18	

Table S2 Comparison electrical conductivity of Sn, Sb and P

Element	Electrical conductivity (S cm^{-1})	Theoretical capacity (mA h g^{-1})
Sn	$9*10^4$	847
Sb	$2.5*10^4$	660
P	$1*10^{-14}$	2596